Gulf Journal of Mathematics
Vol 24, Issue 2 (2026) 1-18

ISSN: 2309-4966
https://doi.org/10.56947/fdy6sz49

A CLOSED TRIGONOMETRIC QUASI-INTERPOLANT FOR FIXED-CENTER RADIAL ACTIVE CONTOURS

AYMAN HIDOU[1], CHAIMAE MOUHOUB[2*] and MOHAMED LAMNII[2]

Abstract. A fixed-center radial description is economical when each ray issued from a prescribed interior point intersects the target boundary once. We formulate an active-contour energy in terms of its periodic radius, retaining the contributions generated by the rotating polar basis in the first- and second-derivative penalties. Edge and region image terms lead to a scalar evolution equation, whose fourth-order part is discretized on a periodic angular grid. To turn the computed samples into a closed curve, we use a local trigonometric quasi-interpolant. We show that this reconstruction joins the endpoint values and first derivatives, reproduces constants and first angular harmonics, and admits third-order function and second-order derivative approximation estimates under the stated smoothness assumptions. An illustrative brain-image example demonstrates the computational workflow. Further experiments with controlled baselines and reported quantitative scores are needed to assess segmentation accuracy and efficiency.

Keywords. Active contour, Kass snake, radial representation, quasi-interpolation, trigonometric splines, image segmentation.
2020 Mathematics Subject Classification. Primary 65D07, 65D18; Secondary 41A15, 68U10

1. Introduction

The boundary of an object can be found by evolving a curve toward features of an image. In the parametric snake introduced by Kass, Witkin and Terzopoulos [8], image forces compete with penalties on variations of the curve. A Cartesian parameterization allows a broad range of shapes, but every update changes two coordinate functions. When the object is known to be star-shaped about an interior point, its boundary can instead be described by one radius for each viewing angle. This restriction is useful in applications with a meaningful center; it excludes boundaries with radial overhangs and makes the choice of center part of the model.

Let c be that fixed center and $e_r(\theta) = (\cos\theta, \sin\theta)^T$. We write the contour as $c + r(\theta)e_r(\theta)$ for a positive 2π-periodic function r. This polar representation has

Date: Received: Sep 27, 2026; Revised: Oct 27, 2026; Accepted: Nov 2, 2026.
* Corresponding author
© The Author(s) 2026. This article is licensed under a Creative Commons Attribution-NonCommercial-NoDerivatives 4.0 International License. To view a copy of the license, visit https://creativecommons.org/licenses/by-nc-nd/4.0/.

a history in curve design [12] and in radial or polar active contours [3, 4, 5, 1]. Star-shape constraints have also been used with other optimization methods [13]. Thus, representing a boundary by angular radii is an established choice. The question addressed here is how to combine an energy-driven update of those radii with a local reconstruction that has a differentiable junction at the angular seam.

Two distinct operations enter the proposed algorithm. First, we restrict a Kass-type energy to radial curves and derive the scalar variation, including terms that arise because the polar basis rotates with θ. The resulting evolution is evaluated at angular grid points using periodic finite differences. Second, after an update of the radius samples, we reconstruct a continuously defined curve by a third-order trigonometric quasi-interpolant. The reconstruction uses nearby samples, including neighbors across $0 \equiv 2\pi$; it therefore requires no global interpolation solve. Its coefficients are chosen to reproduce 1, $\cos\theta$, and $\sin\theta$, while its endpoint relations yield equal first derivatives at the seam.

The mathematical background for trigonometric splines and quasi-interpolation is well established [10, 9, 11]. Quasi-interpolation has also appeared in boundary-detection computations [6], and periodic constructions based on trigonometric B-splines have been studied [7]. Our contribution is the explicit closure-compatible local operator used within the specified radial evolution, together with a derivation of its reproduction and seam properties. We do not claim that either polar snakes or trigonometric quasi-interpolation is new on its own. Contemporary polar instance-segmentation methods [14, 15] provide a different, learned setting and are cited for context rather than used as direct baselines.

The optional region force uses intensity statistics on either side of the curve, in the spirit of region-based active contours [2]. The present numerical illustration contains one annotated brain image and a Cartesian-snake example. Since the examples use different settings and no quantitative scores accompany the source material, they demonstrate implementation rather than a measured improvement. A systematic evaluation must isolate the effects of the radial parameterization and of quasi-interpolation, disclose the image and annotations, and measure accuracy across multiple cases.

Section 2 derives the radial energy and its evolution equation. Section 3 develops the closed quasi-interpolant and its approximation properties. Section 4 describes the periodic discretization, reconstruction cycle, and requirements for a reproducible evaluation. Section 5 summarizes the scope and remaining limitations.

2. From Kass's Snake to the Radial Model

2.1. **Kass's Classical Model.** In the original model by Kass et al. [8], the trajectory is a parametric curve $v : [0,1] \to \mathbb{R}^2$ and the energy is expressed schematically as

$$E_{\text{Kass}}(v) = \int_0^1 \left[\frac{\alpha}{2}\|v'(s)\|^2 + \frac{\beta}{2}\|v''(s)\|^2 + P\big(v(s)\big) \right] ds, \tag{2.1}$$

where $\alpha \geq 0$ controls the tension of the contour, $\beta \geq 0$ its stiffness, and P is a potential dependent on the image, typically decreasing in the vicinity of steep gradients.

The first two terms constitute the internal energy: the term involving v' penalizes rapid variations between neighboring points, while the term involving v'' penalizes strong curvatures and oscillations. The Euler–Lagrange equation associated with (2.1) is

$$-\alpha v_{ss} + \beta v_{ssss} + \nabla P(v) = 0, \tag{2.2}$$

and a gradient flow suitable for numerical minimization is given by

$$\frac{\partial v}{\partial t} = \underbrace{\alpha v_{ss} - \beta v_{ssss}}_{F_{\text{int}}} - \underbrace{\nabla P(v)}_{F_{\text{img}}}.$$

Starting from an initial curve, the variational model updates its location until the image and regularization terms balance. For the fixed-center class considered here, the same variational idea is applied to the angular radius. A constant initial radius specifies a circular initial contour.

2.2. **Radial Parameterization and Moving Polar Basis.** Choose a center c with respect to which the object is star-shaped. We work in translated coordinates so that $c = 0$, and represent the evolving boundary as

$$\Gamma(\theta, t) = r(\theta, t) e_r(\theta), \qquad 0 \leq \theta \leq 2\pi, \tag{2.3}$$

with the moving polar basis

$$e_r(\theta) = \begin{pmatrix} \cos\theta \\ \sin\theta \end{pmatrix}, \qquad e_\theta(\theta) = \begin{pmatrix} -\sin\theta \\ \cos\theta \end{pmatrix}.$$

These polar vectors are orthonormal and rotate with angle according to

$$e_r' = e_\theta, \qquad e_\theta' = -e_r. \tag{2.4}$$

Differentiating the radius and the polar frame together gives

$$\Gamma_\theta = r_\theta e_r + r e_\theta, \tag{2.5}$$

and

$$\Gamma_{\theta\theta} = (r_{\theta\theta} - r) e_r + 2 r_\theta e_\theta. \tag{2.6}$$

By virtue of the orthonormality of (e_r, e_θ),

$$\|\Gamma_\theta\|^2 = r^2 + r_\theta^2, \qquad \|\Gamma_{\theta\theta}\|^2 = (r_{\theta\theta} - r)^2 + 4 r_\theta^2. \tag{2.7}$$

In this parameterization, the perimeter and enclosed area can be calculated from r:

$$L(r) = \int_0^{2\pi} \sqrt{r^2 + r_\theta^2}\, d\theta, \qquad A(r) = \frac{1}{2} \int_0^{2\pi} r(\theta)^2\, d\theta. \tag{2.8}$$

Both geometric quantities are determined by the radius; no separate Cartesian coordinate functions are required within the admissible shape class.

2.3. **Star-Shaped Hypothesis.**

Definition 2.1 (Star-shaped curve)**.** A closed boundary Γ is said to be star-shaped with respect to the origin if, for every $\theta \in \mathbb{T} = \mathbb{R}/2\pi\mathbb{Z}$, the half-line

$$\{\rho e_r(\theta) : \rho \geq 0\}$$

intersects Γ at exactly one point.

Under this assumption, there exists a positive function $r : \mathbb{T} \to \mathbb{R}_+^*$ such that (2.3) describes the contour; related star-shape priors also appear in segmentation models such as [13].

The model cannot therefore represent a ring, two disjoint components, or a shape for which a half-line originating from the center would intersect the contour multiple times. This restriction is both the weakness and the strength of the method: the class of admissible shapes is narrower than in the general Cartesian case, but the scale of the problem and the ambiguities of deformation are thereby considerably reduced.

The choice of origin assumes that the image has been cropped, translated, or described in a coordinate system where the star-shaped reference point coincides with $(0, 0)$; this assumption is deliberate, as this article is studying the fixed-center model. An extension with a variable center—for example, recomputed at each iteration as the centroid of the current contour—is discussed in Section 5.

The natural initialization of the model is a circle:

$$\Gamma^0(\theta) = R_0 e_r(\theta), \qquad \text{that is,} \qquad r^0(\theta) = R_0. \tag{2.9}$$

2.4. **The Role of Geometric Periodicity.**

The two ends of the angular interval correspond to one ray. Closure therefore requires

$$r(0, t) = r(2\pi, t).$$

A continuously joined first derivative additionally requires

$$r_\theta(0, t) = r_\theta(2\pi, t).$$

Since the equation of evolution for the radius established below is of order four in θ, a regular periodic formulation naturally leads us to also consider

$$r_{\theta\theta}(0, t) = r_{\theta\theta}(2\pi, t), \qquad r_{\theta\theta\theta}(0, t) = r_{\theta\theta\theta}(2\pi, t).$$

These conditions prevent the creation, at the point $\theta = 0 \equiv 2\pi$, of an artificial numerical boundary which would introduce an asymmetric treatment of the function r and degrade the apparent regularity of the reconstructed contour.

Periodicity is therefore necessary for the geometric function r. It is, however, not logically necessary for the numerical basis used to represent r: one could choose a basis defined on $[0, 2\pi]$ and impose the above constraints as additional constraints on the boundary coefficients.

However, this solution is less natural in the present context, as it artificially creates asymmetric boundary functions and imposes specific conditions on the first and last coefficients, which unnecessarily complicates the implementation. This is why, in Section 3, we construct a natively periodic quasi-interpolation

operator directly, whose functionals associated with neighboring indices of the closure utilize the identification $2\pi \equiv 0$ explicitly.

2.5. **External Energies in the Radial Frame.** Before deriving the complete equation of evolution for the radius, it is necessary to specify the form, in the radial frame, of the potential P. Two families of external energies are considered: contour energies based on the gradient of the image and region energies based on statistics computed inside and outside the curve.

2.5.1. *Contour Energy.* In line with Kass's original model, the contour potential is constructed from the gradient of the image I, which may be smoothed by a Gaussian kernel G_σ:

$$P_{\text{edge}}(x) = -\left\|\nabla(G_\sigma * I)(x)\right\|^2.$$

Along the radial contour, this potential is evaluated at $x = \Gamma(\theta) = r(\theta)e_r(\theta)$, and the associated image force is the radial projection of the potential gradient,

$$F_r^{\text{edge}}(\theta, t) = -\nabla P_{\text{edge}}\big(\Gamma(\theta, t)\big) \cdot e_r(\theta). \tag{2.10}$$

A perturbation of r moves the point $\Gamma(\theta)$ in direction $e_r(\theta)$, so the first variation retains the radial projection of the image gradient. A tangential perturbation is outside this fixed-angle admissible class.

2.5.2. *Regional Energy.* When local contrast is low, or noise is significant, an energy based solely on the gradient may be insufficiently informative. Following the approach of Chan and Vese [2], one can introduce a region energy that compares a statistic of the interior with that of its exterior.

A simple form is

$$\begin{aligned} E_{\text{reg}}(r) = \int_0^{2\pi} \Bigg[&\int_0^{r(\theta)} \big(I(\rho,\theta) - \mu_{\text{int}}\big)^2 \rho \, d\rho \\ &+ \int_{r(\theta)}^{\rho_{\max}} \big(I(\rho,\theta) - \mu_{\text{ext}}\big)^2 \rho \, d\rho \Bigg] d\theta. \end{aligned} \tag{2.11}$$

Here, $I(\rho, \theta)$ denotes the image expressed in polar coordinates centered on the star point, μ_{int} and μ_{ext} denote the estimated average intensities inside and outside the current contour, and $\rho_{\max}$ denotes a truncation radius determined by the size of the image.

Differentiation with respect to $r(\theta)$ yields

$$F_r^{\text{reg}}(\theta, t) = -\Big[\big(I(r,\theta) - \mu_{\text{int}}\big)^2 - \big(I(r,\theta) - \mu_{\text{ext}}\big)^2\Big] r(\theta, t). \tag{2.12}$$

The sign of the regional force depends on whether the boundary intensity agrees more closely with the estimated interior or exterior intensity. The two means must be recomputed as the contour changes.

2.5.3. *Combined Image Force.* The total radial force is a convex combination of the two contributions:

$$F_r(\theta,t) = (1-\gamma)F_r^{\text{edge}}(\theta,t) + \gamma F_r^{\text{reg}}(\theta,t), \qquad \gamma \in [0,1]. \tag{2.13}$$

The parameter γ allows the model to vary continuously between a purely contour-based radial snake ($\gamma = 0$) and a purely region-based radial snake ($\gamma = 1$).

2.6. **Exact Radial Form of the Internal Energy and Evolution Equation.**

2.6.1. *Total Radial Energy.* We adopt θ as the parameter of the radial functional and substitute $v(\theta) = \Gamma(\theta) = r(\theta)e_r(\theta)$ into the internal regularization terms.

If one starts from the normalized parameter $s \in [0,1]$ and sets $\theta = 2\pi s$, the corresponding powers of 2π are absorbed into rescaled regularization parameters α and β.

The radial internal energy is

$$E_{\text{int}}^{\text{rad}}(r) = \frac{1}{2}\int_0^{2\pi} \left[\alpha(r_\theta^2 + r^2) + \beta\big((r_{\theta\theta} - r)^2 + 4r_\theta^2\big)\right] d\theta. \tag{2.14}$$

For the contour contribution, we set

$$E_{\text{edge}}(r) = \int_0^{2\pi} P_{\text{edge}}\big(r(\theta)e_r(\theta)\big)\, d\theta.$$

When the regional contribution is included, the total radial energy is

$$E_{\text{rad}}(r) = E_{\text{int}}^{\text{rad}}(r) + (1-\gamma)E_{\text{edge}}(r) + \gamma E_{\text{reg}}(r). \tag{2.15}$$

The terms containing r explicitly in the internal energy arise from the rotation of the polar basis when differentiating $re_r(\theta)$.

2.6.2. *Euler–Lagrange Equation for the Radius.* For a local contour potential P_{edge}, let

$$\mathcal{L}(r, r_\theta, r_{\theta\theta}) = \frac{\alpha}{2}(r_\theta^2 + r^2) + \frac{\beta}{2}\left[(r_{\theta\theta} - r)^2 + 4r_\theta^2\right] + P_{\text{edge}}(re_r).$$

For a Lagrangian dependent on $r_{\theta\theta}$, the generalized Euler–Lagrange equation is

$$\frac{\partial \mathcal{L}}{\partial r} - \frac{d}{d\theta}\left(\frac{\partial \mathcal{L}}{\partial r_\theta}\right) + \frac{d^2}{d\theta^2}\left(\frac{\partial \mathcal{L}}{\partial r_{\theta\theta}}\right) = 0. \tag{2.16}$$

We successively compute

$$\begin{aligned} \frac{\partial \mathcal{L}}{\partial r} &= (\alpha+\beta)r - \beta r_{\theta\theta} + \nabla P_{\text{edge}}(\Gamma)\cdot e_r, \\ \frac{\partial \mathcal{L}}{\partial r_\theta} &= (\alpha + 4\beta)r_\theta, \\ \frac{\partial \mathcal{L}}{\partial r_{\theta\theta}} &= \beta(r_{\theta\theta} - r). \end{aligned} \tag{2.17}$$

Substitution gives

$$\beta r_{\theta\theta\theta\theta} - (\alpha + 6\beta)r_{\theta\theta} + (\alpha+\beta)r + \nabla P_{\text{edge}}(\Gamma)\cdot e_r = 0. \tag{2.18}$$

For the combined contour-and-region model, the associated gradient flow is therefore

$$r_t = (\alpha + 6\beta)r_{\theta\theta} - \beta r_{\theta\theta\theta\theta} - (\alpha + \beta)r + F_r. \tag{2.19}$$

If $F_r > 0$, the radius increases locally; if $F_r < 0$, the contour moves closer to the center.

Remark 2.2. The radial equation is formally a fourth-order scalar equation on the circle $\mathbb{T}$. The radial framework reduces the unknown from two coupled Cartesian functions (x, y) to a single scalar function r, using N scalar unknowns instead of $2N$ Cartesian coordinates for the same number of contour nodes.

3. Closed Third-Order Trigonometric Quasi-Interpolation

We now specify a local reconstruction whose coefficients account for angular wraparound. It reproduces the low-frequency trigonometric space and joins both the radius and its first derivative at $0 \equiv 2\pi$. The construction uses trigonometric B-splines and their Marsden identities [10, 11].

3.1. **Third-Order Trigonometric Space.**

For $k = 3$, the associated trigonometric space is

$$\mathcal{T}_3 = \operatorname{span}\{1, \cos\theta, \sin\theta\}.$$

A constant radius yields a circle, while the sine and cosine terms provide the first angular modes of radius variation.

We consider a uniform subdivision

$$\theta_j = jh, \qquad h = \frac{2\pi}{N}, \qquad j = 0, \dots, N, \qquad 0 < h < \pi.$$

For the representation on $[0, 2\pi]$, we use the sequence of third-order nodes, of multiplicity three at the endpoints,

$$0 = t_1 = t_2 = t_3 < t_4 < \cdots < t_{m+1} = t_{m+2} = t_{m+3} = 2\pi.$$

For the uniform grid above, the $N - 1$ interior simple knots imply $m = N + 2$.

3.2. **Third-Order Trigonometric B-Splines.**

The recurrence relation defining trigonometric B-splines is

$$T_{i,1}(x) = \begin{cases} 1, & t_i \le x < t_{i+1}, \\ 0, & \text{otherwise}, \end{cases}$$

and, for $k \ge 2$,

$$\begin{aligned} T_{i,k}(x) = {} & \frac{\sin\big((x - t_i)/2\big)}{\sin\big((t_{i+k-1} - t_i)/2\big)} T_{i,k-1}(x) \\ & + \frac{\sin\big((t_{i+k} - x)/2\big)}{\sin\big((t_{i+k} - t_{i+1})/2\big)} T_{i+1,k-1}(x), \end{aligned} \tag{3.1}$$

with the convention that a term whose denominator vanishes is taken to be zero [10, 11].

On a uniform mesh, any interior B-spline of order three is a translation of the same parent spline. By choosing the reference support $[0, 3h]$, we obtain

$$\Phi_3(x) = \begin{cases} \dfrac{\sin^2(x/2)}{\sin h\, \sin(h/2)}, & 0 \le x < h, \\ \dfrac{\sin(x/2)\sin((2h-x)/2) + \sin((3h-x)/2)\sin((x-h)/2)}{\sin h\, \sin(h/2)}, & h \le x < 2h, \\ \dfrac{\sin^2((3h-x)/2)}{\sin h\, \sin(h/2)}, & 2h \le x \le 3h, \\ 0, & \text{otherwise.} \end{cases} \tag{3.2}$$

The central segment can also be written in condensed form

$$\Phi_3(x) = \frac{\cos(h/2)\cos(x - 3h/2) - \cos h}{\sin h\, \sin(h/2)}, \qquad h \le x < 2h.$$

Thus, for the interior splines,

$$T_{i,3}(x) = \Phi_3(x - t_i).$$

3.3. **Trigonometric Marsden Identity.** The trigonometric Marsden identities identify the spline coefficients of the three functions spanning $\mathcal{T}_3$ [10, 11]:

$$1 = \sum_i \cos\left(\frac{t_{i+1} - t_{i+2}}{2}\right) T_{i,3}(x), \tag{3.3}$$

$$\cos x = \sum_i \cos\left(\frac{t_{i+1} + t_{i+2}}{2}\right) T_{i,3}(x), \tag{3.4}$$

$$\sin x = \sum_i \sin\left(\frac{t_{i+1} + t_{i+2}}{2}\right) T_{i,3}(x). \tag{3.5}$$

We choose each local functional to match those coefficients when applied to 1, cos, and sin. Write

$$c_h = \cos(h/2), \qquad s_h = \sin(h/2).$$

3.4. **Interior Functionals and Closure Correction.** For interior indices $i = 3, \dots, m-2$, we use the local functional

$$\lambda_i(f) = \frac{1}{4c_h}\left[-f\big((i-3)h\big) + 2(1+\cos h) f\big((i-2)h\big) + f\big((i-1)h\big)\right]. \tag{3.6}$$

For a closed contour, the points 0 and 2π represent the same geometric point. We therefore assume

$$f(0) = f(2\pi). \tag{3.7}$$

We retain

$$\lambda_1^c(f) = f(0), \qquad \lambda_m^c(f) = f(2\pi) = f(0),$$

but the two functionals adjacent to the closure are

$$\begin{aligned}\lambda_2^c(f) &= c_h f(0) + \frac{f(h) - f(2\pi - h)}{4c_h},\\ \lambda_{m-1}^c(f) &= c_h f(0) - \frac{f(h) - f(2\pi - h)}{4c_h}.\end{aligned} \tag{3.8}$$

The sample at $2\pi - h$ is adjacent to those at 0 and h on the circle, so both endpoint functionals remain local.

3.5. **Derivation of the Closure Functionals from Marsden.** For $T_{2,3}$, the Marsden coefficients associated with 1, $\cos x$, and $\sin x$ are c_h, c_h, and s_h, respectively. We seek

$$\lambda_2^c(f) = Af(2\pi - h) + Bf(0) + Cf(h).$$

The reproduction conditions give

$$\begin{cases} A + B + C = c_h,\\ (A + C)\cos h + B = c_h,\\ (C - A)\sin h = s_h, \end{cases}$$

whose unique solution is

$$A = -\frac{1}{4c_h}, \qquad B = c_h, \qquad C = \frac{1}{4c_h}.$$

For $T_{m-1,3}$, the coefficient of $\sin x$ changes sign since

$$\sin(2\pi - h/2) = -s_h,$$

which yields the expression for λ_{m-1}^c. In particular,

$$\lambda_2^c(f) + \lambda_{m-1}^c(f) = 2c_h f(0). \tag{3.9}$$

3.6. **Closed Quasi-Interpolant and Fundamental Properties.**

Theorem 3.1 (Closed Trigonometric Quasi-Interpolant of Order Three)**.** *Let $f \in C^1([0, 2\pi])$ satisfy $f(0) = f(2\pi)$. Define*

$$Q_{3,h}^c f(x) = \sum_{i=1}^{m} \lambda_i^c(f) T_{i,3}(x),$$

where the interior and closure functionals are those defined above. Then:

(i) $Q_{3,h}^c$ is linear and local on the circle;
(ii) $Q_{3,h}^c p = p$ for every $p \in \mathcal{T}_3 = \operatorname{span}\{1, \cos x, \sin x\}$;
(iii) $Q_{3,h}^c f(0) = Q_{3,h}^c f(2\pi)$;
(iv)

$$(Q_{3,h}^c f)'(0^+) = (Q_{3,h}^c f)'(2\pi^-).$$

Thus, $Q_{3,h}^c f$ defines a C^1 function on $\mathbb{T} = \mathbb{R}/2\pi\mathbb{Z}$.

Proof. Every coefficient is a linear combination of nearby samples, with the neighbors at the seam interpreted periodically. Substitution of each basis function of $\mathcal{T}_3$ into the functionals gives its Marsden coefficients, proving reproduction by linearity.

The endpoint values of the open-knot B-splines are

$$T_{1,3}(0) = 1, \qquad T_{i,3}(0) = 0 \quad (i \neq 1),$$

and symmetrically

$$T_{m,3}(2\pi) = 1, \qquad T_{i,3}(2\pi) = 0 \quad (i \neq m).$$

Thus,

$$Q^c_{3,h} f(0) = f(0), \qquad Q^c_{3,h} f(2\pi) = f(2\pi).$$

For the derivatives at the boundary, the recursion formula gives

$$T'_{1,3}(0^+) = -\cot(h/2), \qquad T'_{2,3}(0^+) = \csc(h/2),$$

and

$$T'_{m-1,3}(2\pi^-) = -\csc(h/2), \qquad T'_{m,3}(2\pi^-) = \cot(h/2).$$

Therefore,

$$\begin{aligned} (Q^c_{3,h} f)'(0^+) &= \frac{\lambda^c_2(f) - c_h f(0)}{s_h}, \\ (Q^c_{3,h} f)'(2\pi^-) &= \frac{c_h f(0) - \lambda^c_{m-1}(f)}{s_h}. \end{aligned} \tag{3.10}$$

The identity

$$\lambda^c_2(f) + \lambda^c_{m-1}(f) = 2c_h f(0)$$

shows that the two quantities are equal. More precisely,

$$(Q^c_{3,h} f)'(0) = (Q^c_{3,h} f)'(2\pi) = \frac{f(h) - f(2\pi - h)}{2\sin h}. \tag{3.11}$$

□

Remark 3.2. The last formula is a trigonometric centered difference at the closure point. It is exact on $\mathcal{T}_3$: for $f(x) = \sin x$, it gives $1 = f'(0)$, and for $f(x) = \cos x$, it gives $0 = f'(0)$.

3.7. **Approximation Error.** The space $\mathcal{T}_3$ is the kernel of the differential operator

$$L_3 = D(D^2 + 1) = D^3 + D.$$

The theory of Lyche, Schumaker, and Stanley establishes optimal-order estimates for trigonometric quasi-interpolants reproducing $\mathcal{T}_\ell$, relying on a trigonometric Taylor expansion and its remainder [11].

Proposition 3.3 (Order of Approximation)**.** *Let $f \in W^{3,\infty}(\mathbb{T})$ be 2π-periodic and let $0 < h \leq h_0 < \pi$. Assume that the functionals of $Q^c_{3,h}$ are uniformly bounded for such a family of meshes. Then there exist constants $C_0, C_1 > 0$, independent of h, such that*

$$\|f - Q^c_{3,h} f\|_\infty \leq C_0 h^3 \|L_3 f\|_\infty,$$

and

$$\|f' - (Q^c_{3,h} f)'\|_\infty \le C_1 h^2 \|L_3 f\|_\infty.$$

The respective rates are $O(h^3)$ and $O(h^2)$.

Proof. Subtract from f its local trigonometric Taylor expansion $U_{3,t} f \in \mathcal{T}_3$. Since $Q^c_{3,h}$ leaves $\mathcal{T}_3$ invariant, the reproduced term vanishes in the difference and the error depends only on the remainder.

This remainder is controlled by

$$L_3 f = (D^3 + D) f.$$

On a support of diameter $O(h)$, the remainder is of order h^3. Differentiating a B-spline lowers this order by one power of h, yielding order two for the derivative. The modified closure templates remain local and uniformly bounded for $h \le h_0 < \pi$, so the same argument applies at the periodic boundary. □

4. Discretization, Algorithmic Coupling, and Numerical Validation

4.1. **Discrete Approximation of the Radial Evolution.** Let the angular variable be sampled on the uniform periodic grid

$$\theta_j = jh, \qquad h = \frac{2\pi}{N}, \qquad j = 0, \dots, N-1,$$

and denote by

$$r^n = (r^n_0, \dots, r^n_{N-1})^T$$

the vector of radial values at iteration n.

The indices are understood modulo N, so that the discrete operators naturally preserve periodicity.

The second angular derivative is approximated by

$$(D^2 r)_j = \frac{r_{j+1} - 2r_j + r_{j-1}}{h^2},$$

whereas the fourth derivative is represented by

$$(D^4 r)_j = \frac{r_{j-2} - 4r_{j-1} + 6r_j - 4r_{j+1} + r_{j+2}}{h^4}. \tag{4.1}$$

Because the angular domain is periodic, the same formulas are used at every grid point. No additional boundary formulas are required near $\theta = 0$ and $\theta = 2\pi$.

Using these discrete operators, a first-order explicit approximation of (2.19) is

$$\begin{aligned} \widetilde{r}^{n+1} = r^n + \tau \Big[&(\alpha + 6\beta) D^2 r^n - \beta D^4 r^n \\ &- (\alpha + \beta) r^n + F^n_r \Big], \end{aligned} \tag{4.2}$$

where $\tau > 0$ is the time increment and F^n_r collects the radial external forces evaluated on the contour at iteration n.

Remark 4.1. The fourth-order contribution imposes a restrictive stability condition on a fully explicit implementation. In particular, the admissible time step typically satisfies

$$\tau = \mathcal{O}\left(\frac{h^4}{\beta}\right).$$

For fine angular meshes, this restriction may considerably increase the number of iterations.

A convenient alternative consists in treating the linear terms involving D^2 and D^4 implicitly while keeping the external force explicit. We therefore use the semi-implicit update

$$\left[I - \tau(\alpha + 6\beta)D^2 + \tau\beta D^4 + \tau(\alpha + \beta)I\right]\widetilde{r}^{n+1} = r^n + \tau F_r^n. \tag{4.3}$$

Because D^2 and D^4 are periodic circulant matrices, the resulting linear system can be solved efficiently at every iteration, including by Fourier-based methods.

4.2. **Coupling with the Closed Quasi-Interpolation Operator.** The predictor $\widetilde{r}^{n+1}$ contains radial values defined only at the angular nodes. A continuous representation is therefore introduced before constructing the updated contour.

The closed trigonometric quasi-interpolation operator is applied at every iteration:

$$r_h^{n+1}(\theta) = Q_{3,h}^c \widetilde{r}^{n+1}(\theta). \tag{4.4}$$

Since $Q_{3,h}^c$ is a quasi-interpolant, the reconstructed function does not necessarily interpolate the predictor values exactly. The discrete data entering the next iteration are consequently obtained by resampling:

$$r_j^{n+1} = r_h^{n+1}(\theta_j), \qquad j = 0, \dots, N-1.$$

The corresponding closed contour is

$$\Gamma_h^{n+1}(\theta) = r_h^{n+1}(\theta) e_r(\theta).$$

The transition between two successive iterations may be summarized as

$$\begin{aligned} r^n &\longrightarrow \widetilde{r}^{n+1} \longrightarrow r_h^{n+1} \\ &\longrightarrow r^{n+1} \longrightarrow \Gamma_h^{n+1}. \end{aligned}$$

4.3. **Contribution of the Quasi-Interpolant.** The predictor and the quasi-interpolation stage have different numerical roles. The predictor contains the discretized variational dynamics, whereas $Q_{3,h}^c$ provides a smooth periodic reconstruction. Nevertheless, reconstruction can influence later iterations because the resulting function is sampled again.

The closed quasi-interpolant has the following main purposes:

- to reconstruct the radial function locally from discrete samples without solving a global interpolation problem;
- to preserve the required C^1 matching at the periodic junction $\theta = 0 \equiv 2\pi$;
- to reproduce the modes

$$1, \qquad \cos\theta, \qquad \sin\theta;$$

- to provide a smooth representation of the contour for the evaluation of image-dependent quantities at the next iteration.

In particular, reproduction of constants gives

$$Q^c_{3,h} R_0 = R_0.$$

Therefore, a circle of constant radius R_0 is left unchanged by the reconstruction step alone. Higher angular modes may, however, be modified by repeated reconstruction and resampling.

4.4. **Treatment of the Fourth-Order Contribution.** The C^1 closure supplied by the quasi-interpolant is sufficient for the geometric representation considered here. It should not, however, be interpreted as a means of evaluating the fourth derivative appearing in the radial evolution equation.

The quantity

$$r_{\theta\theta\theta\theta}$$

is not obtained by differentiating r^n_h four times. Instead, the fourth-order contribution is computed directly from the discrete radius vector using the periodic operator D^4.

Thus,

$$D^4 \quad \text{approximates the fourth-order differential term,}$$

whereas

$$Q^c_{3,h} \quad \text{reconstructs the updated closed contour.}$$

This distinction is important because C^1 regularity alone does not provide the classical fourth-order smoothness required for a pointwise evaluation of $r_{\theta\theta\theta\theta}$.

4.5. **Algorithmic Procedure.** The computation starts from a circular initialization,

$$r^0_j = R_0, \qquad j = 0, \dots, N-1.$$

At iteration n, the following operations are performed:

(1) Construct the current contour:

$$\Gamma^n_h(\theta) = r^n_h(\theta) e_r(\theta).$$

(2) Evaluate the radial edge contribution $F^{\mathrm{edge},n}_{r,j}$ according to (2.10), together with the regional contribution $F^{\mathrm{reg},n}_{r,j}$ defined in (2.12).

(3) Form the combined external force:

$$F^n_{r,j} = (1-\gamma) F^{\mathrm{edge},n}_{r,j} + \gamma F^{\mathrm{reg},n}_{r,j}.$$

(4) Advance the radial dynamics to obtain $\widetilde{r}^{n+1}$ using the explicit or semi-implicit update.

(5) Reconstruct the updated radial function:

$$r^{n+1}_h = Q^c_{3,h} \widetilde{r}^{n+1},$$

and sample it at the grid points:

$$r^{n+1}_j = r^{n+1}_h(\theta_j).$$

(6) Form the new closed contour:

$$\Gamma_h^{n+1}(\theta) = r_h^{n+1}(\theta) e_r(\theta).$$

(7) Continue until

$$\frac{\|r^{n+1} - r^n\|_\infty}{\max\{1, \|r^n\|_\infty\}} < \varepsilon.$$

For an image defined on a bounded domain, the admissible radius must remain positive and inside the image support. If clipping, projection, or another constraint-handling procedure is employed, it should be explicitly stated.

4.6. **Numerical Verification of the Reconstruction Order.** Before considering image segmentation, we verify independently the approximation behavior of the closed quasi-interpolant. We use the smooth 2π-periodic test function

$$f(\theta) = 2 + 0.3\cos(2\theta) + 0.2\sin(3\theta), \tag{4.5}$$

which is not contained in $\mathcal{T}_3$ and therefore provides a nontrivial reconstruction test.

For successive uniform grids, we compute

$$E_0 = \|f - Q_{3,h}^c f\|_\infty, \qquad E_1 = \|f' - (Q_{3,h}^c f)'\|_\infty,$$

and the observed order

$$\log_2 \left(\frac{E(h)}{E(h/2)} \right).$$

The errors are evaluated on a dense uniform angular grid.

Table 1. Convergence of the closed trigonometric quasi-interpolant for the periodic test function.

N	E_0	Order	E_1	Order
20	2.4146×10^{-2}	–	9.7271×10^{-2}	–
40	3.2269×10^{-3}	2.904	3.6979×10^{-2}	1.395
80	4.0936×10^{-4}	2.979	9.9888×10^{-3}	1.888
160	5.1419×10^{-5}	2.993	2.5109×10^{-3}	1.992
320	6.4337×10^{-6}	2.999	6.2403×10^{-4}	2.009

The function error approaches third order, whereas the derivative error approaches second order as the grid is refined. These observations are consistent with the theoretical approximation orders and indicate that the closure correction does not degrade the observed asymptotic behavior.

4.7. **Illustrative Numerical Experiment and Reproducibility.** The numerical illustration is based on a single brain image together with a manually specified reference contour. Figure 1 displays the input image and its reference annotation when the corresponding file is available.

This experiment illustrates the numerical behavior of the proposed construction. A single image is not sufficient to establish general conclusions regarding segmentation accuracy or robustness.

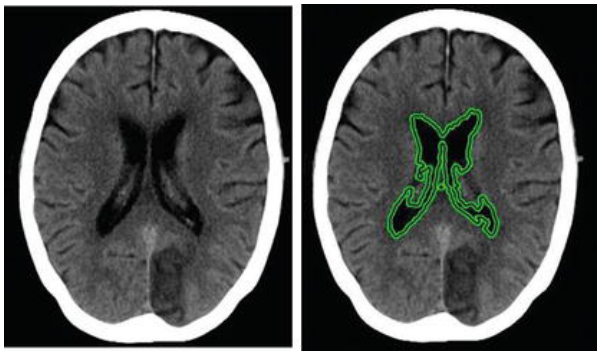


Figure 1. Input brain slice with the reference annotation.

A reproducible study should specify the image dimensions, spatial resolution, annotation procedure, intensity preprocessing, and the center used for the radial parametrization.

For the radial experiment, the parameters are

$$N = 180, \qquad \alpha = 3.35 \times 10^{-3}, \qquad \beta = 1.36 \times 10^{-4},$$
$$\tau = 0.25, \qquad \gamma = 0.79.$$

The external-force gain is 20.5, and the maximum number of iterations is 220.

The implementation uses a semi-implicit evolution step followed by closed quasi-interpolation and resampling. Figure 2 illustrates the resulting radial contour when the corresponding output is available.

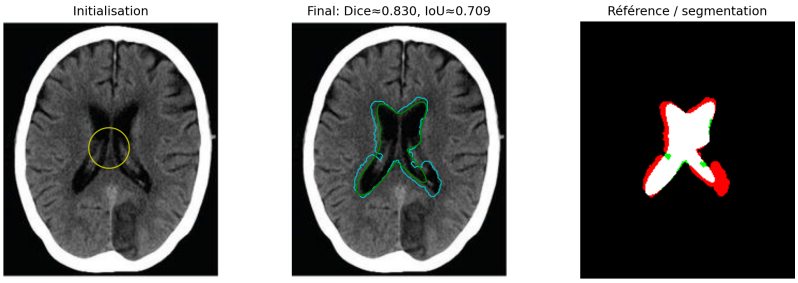


Figure 2. Radial segmentation result and reference contour.

The parameters listed above are not sufficient, by themselves, for complete reproduction of the experiment. The evaluation of image forces, image interpolation, initialization center, initial radius, preprocessing, stopping tolerance, intensity normalization, updating of regional statistics, and radius constraints should also be documented.

For reference, the Cartesian Kass-snake experiment uses

$$N = 240, \qquad \alpha = 5 \times 10^{-3}, \qquad \beta = 10^{-1},$$
$$\tau = 0.40.$$

The line and edge weights are 0.50 and 2.00, respectively. The external-force gain is 2.50, and the maximum number of iterations is 700.

These parameters, the number of contour nodes, and the definition of the image force differ from those used in the radial experiment. Consequently, the two numerical outputs should be interpreted as separate illustrations rather than as a controlled quantitative comparison.

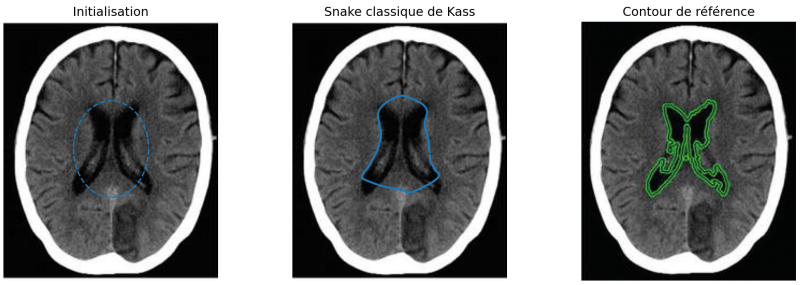


Figure 3. Cartesian snake result with its reference contour.

The present image experiment is intended to illustrate the complete numerical workflow rather than to serve as a quantitative benchmark. A broader validation should use a common experimental protocol and report complementary region- and boundary-based measures, such as the Dice coefficient, intersection over union, Hausdorff distance, average symmetric surface distance, and computational time.

5. Conclusion and Perspectives

A star-shaped contour can be evolved through a periodic scalar radius once an interior center has been fixed. Restricting the parameter-dependent Kass energy to this representation gives a fourth-order radial equation with additional radius terms arising from the rotating polar frame. We evaluated those derivatives on a periodic grid and used a local trigonometric quasi-interpolant to reconstruct the curve after each update. The operator reproduces the constant and first harmonic modes and provides matching values and first derivatives at the angular seam. The stated approximation orders concern reconstruction of sufficiently smooth periodic data; they do not, by themselves, imply a corresponding segmentation accuracy.

The reconstruction experiment confirms the expected third-order function approximation and second-order derivative approximation on successively refined periodic grids. The brain-image example illustrates the complete coupling between radial evolution, periodic discretization, and closed reconstruction. Since the Cartesian example uses a different force definition, discretization size, and iteration budget, it is retained only as a qualitative reference rather than as evidence of superiority. Future work will focus on controlled multi-image validation, sensitivity to center placement, positivity-preserving radius constraints, and extensions beyond a single fixed star center.

References

[1] Bessa, J. A., Cortez, P. C., da Silva Félix, J. H., da Rocha Neto, A. R., & de Alexandria, A. R. (2015). Radial snakes: Comparison of segmentation methods in synthetic noisy

images. *Expert Systems with Applications, 42*, 3079–3088. https://doi.org/10.1016/j.eswa.2014.11.036.

[2] Chan, T. F., & Vese, L. A. (2001). Active contours without edges. *IEEE Transactions on Image Processing, 10*, 266–277. https://doi.org/10.1109/83.902291.

[3] Chen, Y., Huang, T. S., & Rui, Y. (2001). Optimal radial contour tracking by dynamic programming. In *Proceedings of the IEEE International Conference on Image Processing* (pp. 626–629). https://doi.org/10.1109/ICIP.2001.959123.

[4] Collewet, C. (2009). Polar snakes: A fast and robust parametric active contour model. In *Proceedings of the IEEE International Conference on Image Processing* (pp. 3013–3016). https://doi.org/10.1109/ICIP.2009.5414444.

[5] de Alexandria, A. R., Cortez, P. C., Bessa, J. A., da Silva Félix, J. H., de Abreu, J. S., & de Albuquerque, V. H. C. (2014). pSnakes: A new radial active contour model and its application in the segmentation of the left ventricle from echocardiographic images. *Computer Methods and Programs in Biomedicine, 116*, 260–273. https://doi.org/10.1016/j.cmpb.2014.05.009.

[6] Gao, Q., Wu, Z., & Zhang, S. (2011). Applying multiquadric quasi-interpolation for boundary detection. *Computers & Mathematics with Applications, 62*, 4356–4361. https://doi.org/10.1016/j.camwa.2011.09.069.

[7] Gao, W., & Wu, Z. (2014). A quasi-interpolation scheme for periodic data based on multiquadric trigonometric B-splines. *Journal of Computational and Applied Mathematics, 271*, 20–30. https://doi.org/10.1016/j.cam.2014.03.012.

[8] Kass, M., Witkin, A., & Terzopoulos, D. (1988). Snakes: Active contour models. *International Journal of Computer Vision, 1*, 321–331. https://doi.org/10.1007/BF00133570.

[9] Koch, P. E., Lyche, T., Neamtu, M., & Schumaker, L. L. (1995). Control curves and knot insertion for trigonometric splines. *Advances in Computational Mathematics, 3*, 405–424. https://doi.org/10.1007/BF03028369.

[10] Lyche, T., & Winther, R. (1979). A stable recurrence relation for trigonometric B-splines. *Journal of Approximation Theory, 25*, 266–279. https://doi.org/10.1016/0021-9045(79)90017-0.

[11] Lyche, T., Schumaker, L. L., & Stanley, S. (1998). Quasi-interpolants based on trigonometric splines. *Journal of Approximation Theory, 95*, 280–309. https://doi.org/10.1006/jath.1998.3196.

[12] S
'anchez-Reyes, J. (1990). Single-valued curves in polar coordinates. *Computer-Aided Design, 22*, 19–26.

[13] Veksler, O. (2008). Star shape prior for graph-cut image segmentation. In D. Forsyth, P. Torr, & A. Zisserman (Eds.), *Computer Vision – ECCV 2008* (Lecture Notes in Computer Science, Vol. 5304, pp. 454–467). Springer. https://doi.org/10.1007/978-3-540-88690-7_34.

[14] Xie, E., Sun, P., Song, X., Wang, W., Liu, X., Liang, D., Shen, C., & Luo, P. (2020). PolarMask: Single shot instance segmentation with polar representation. In *Proceedings of the IEEE/CVF Conference on Computer Vision and Pattern Recognition* (pp. 12193–12202).

[15] Xu, W., Wang, H., Qi, F., & Lu, C. (2019). Explicit shape encoding for real-time instance segmentation. In *Proceedings of the IEEE/CVF International Conference on Computer Vision* (pp. 5168–5177).

[1] Laboratory LACSI2A, Oujda, Morocco.
Email address: Aymanhidou01@gmail.com

[2] University Mohammed First, Laboratory LACSI2A, Faculty of Sciences, Oujda, Morocco.
Email address: chaimae.mouhoub.d24@ump.ac.ma

[2] University Mohammed First, Laboratory LACSI2A, Faculty of Sciences, Oujda, Morocco.

Email address: lamnii.mohamed@ump.ac.ma